Research Article | Vol. 7, No. 10 | 1 Oct 2016 | BIOMEDICAL OPTICS EXPRESS 4228
Biomedical Optics EXPRESS

Label free measurement of retinal blood cell flux, velocity, hematocrit and capillary width in the living mouse eye

A. GUEVARA-TORRES,[1,2,*] A. JOSEPH,[1,2] AND J. B. SCHALLEK[1,3,4]

[1]*Center for Visual Science, University of Rochester, Rochester, NY 14627, USA*
[2]*The Institute of Optics, University of Rochester, Rochester, NY 14620, USA*
[3]*Flaum Eye Institute, University of Rochester, Rochester, NY 14642, USA*
[4]*Department of Neuroscience, University of Rochester, Rochester, NY 14642, USA*
[*]*rguevara@optics.rochester.edu*

Abstract: Measuring blood cell dynamics within the capillaries of the living eye provides crucial information regarding the health of the microvascular network. To date, the study of single blood cell movement in this network has been obscured by optical aberrations, hindered by weak optical contrast, and often required injection of exogenous fluorescent dyes to perform measurements. Here we present a new strategy to non-invasively image single blood cells in the living mouse eye without contrast agents. Eye aberrations were corrected with an adaptive optics camera coupled with a fast, 15 kHz scanned beam orthogonal to a capillary of interest. Blood cells were imaged as they flowed past a near infrared imaging beam to which the eye is relatively insensitive. Optical contrast of cells was optimized using differential scatter of blood cells in the split-detector imaging configuration. Combined, these strategies provide label-free, non-invasive imaging of blood cells in the retina as they travel in single file in capillaries, enabling determination of cell flux, morphology, class, velocity, and rheology at the single cell level.

OCIS codes: (170.4460) Ophthalmic optics and devices; (330.4300) Vision system - noninvasive assessment; (110.1080) Active or adaptive optics; (330.7324) Visual optics, comparative animal models

References and links

1. D. G. Lyons, A. Parpaleix, M. Roche, and S. Charpak, "Mapping oxygen concentration in the awake mouse brain," eLife **5**, e12024 (2016).
2. P. Lennie, "The Cost of Cortical Computation," Curr. Biol. **13**(6), 493–497 (2003).
3. M. T. T. Wong-Riley, "Energy metabolism of the visual system," Eye Brain **2**, 99–116 (2010).
4. W. H. Organization, *Prevention of Blindness from Diabetes Mellitus: Report of a WHO Consultation in Geneva, Switzerland, 9–11 November 2005* (World Health Organization, 2006).
5. D. S. Fong, L. P. Aiello, F. L. Ferris 3rd, and R. Klein, "Diabetic Retinopathy," Diabetes Care **27**(10), 2540–2553 (2004).
6. R. Klein, B. E. K. Klein, S. E. Moss, M. D. Davis, and D. L. DeMets, "The Wisconsin Epidemiologic Study of Diabetic Retinopathy. III. Prevalence and Risk of Diabetic Retinopathy When Age at Diagnosis Is 30 or More Years," Arch. Ophthalmol. **102**(4), 527–532 (1984).
7. R. Klein, B. E. Klein, S. E. Moss, M. D. Davis, and D. L. DeMets, "The Wisconsin epidemiologic study of diabetic retinopathy. IV. Diabetic macular edema," Ophthalmology **91**(12), 1464–1474 (1984).
8. Y. Akagi-Kurashige, A. Tsujikawa, S. Ooto, Y. Makiyama, Y. Muraoka, K. Kumagai, A. Uji, S. Arichika, T. Murakami, K. Miyamoto, and N. Yoshimura, "Retinal Microstructural Changes in Eyes With Resolved Branch Retinal Vein Occlusion: An Adaptive Optics Scanning Laser Ophthalmoscopy Study," Am. J. Ophthalmol. **157**(6), 1239–1249 (2014).
9. D. A. Antonetti, R. Klein, and T. W. Gardner, "Diabetic Retinopathy," N. Engl. J. Med. **366**(13), 1227–1239 (2012).
10. D. G. Cogan, D. Toussaint, and T. Kuwabara, "Retinal vascular patterns. IV. Diabetic retinopathy," Arch. Ophthalmol. **66**(3), 366–378 (1961).
11. J. Lee, W. Wu, F. Lesage, and D. A. Boas, "Multiple-capillary measurement of RBC speed, flux, and density with optical coherence tomography," J. Cereb. Blood Flow Metab. **33**(11), 1707–1710 (2013).
12. I. H. Sarelius and B. R. Duling, "Direct measurement of microvessel hematocrit, red cell flux, velocity, and transit time," Am. J. Physiol. **243**(6), H1018–H1026 (1982).

#269611 http://dx.doi.org/10.1364/BOE.7.004228
Journal © 2016 Received 11 Jul 2016; revised 19 Sep 2016; accepted 20 Sep 2016; published 23 Sep 2016

Biomedical Optics EXPRESS

13. D. Kleinfeld, P. P. Mitra, F. Helmchen, and W. Denk, "Fluctuations and stimulus-induced changes in blood flow observed in individual capillaries in layers 2 through 4 of rat neocortex," Proc. Natl. Acad. Sci. U.S.A. **95**(26), 15741–15746 (1998).
14. A. Y. Shih, J. D. Driscoll, P. J. Drew, N. Nishimura, C. B. Schaffer, and D. Kleinfeld, "Two-Photon Microscopy as a Tool to Study Blood Flow and Neurovascular Coupling in the Rodent Brain," J. Cereb. Blood Flow Metab. **32**(7), 1277–1309 (2012).
15. J. Nguyen, N. Nishimura, R. N. Fetcho, C. Iadecola, and C. B. Schaffer, "Occlusion of cortical ascending venules causes blood flow decreases, reversals in flow direction, and vessel dilation in upstream capillaries," J. Cereb. Blood Flow Metab. **31**(11), 2243–2254 (2011).
16. J. Liang, D. R. Williams, and D. T. Miller, "Supernormal vision and high-resolution retinal imaging through adaptive optics," J. Opt. Soc. Am. A **14**(11), 2884–2892 (1997).
17. J. Porter, *Adaptive Optics for Vision Science: Principles, Practices, Design, and Applications* (John Wiley and Sons, 2006).
18. J. L. McWhirter, H. Noguchi, and G. Gompper, "Flow-induced clustering and alignment of vesicles and red blood cells in microcapillaries," Proc. Natl. Acad. Sci. U.S.A. **106**(15), 6039–6043 (2009).
19. J. A. Martin and A. Roorda, "Direct and noninvasive assessment of parafoveal capillary leukocyte velocity," Ophthalmology **112**(12), 2219–2224 (2005).
20. Z. Zhong, B. L. Petrig, X. Qi, and S. A. Burns, "*In vivo* measurement of erythrocyte velocity and retinal blood flow using adaptive optics scanning laser ophthalmoscopy," Opt. Express **16**(17), 12746–12756 (2008).
21. Z. Zhong, H. Song, T. Y. P. Chui, B. L. Petrig, and S. A. Burns, "Noninvasive measurements and analysis of blood velocity profiles in human retinal vessels," Invest. Ophthalmol. Vis. Sci. **52**(7), 4151–4157 (2011).
22. J. Tam, P. Tiruveedhula, and A. Roorda, "Characterization of single-file flow through human retinal parafoveal capillaries using an adaptive optics scanning laser ophthalmoscope," Biomed. Opt. Express **2**(4), 781–793 (2011).
23. P. Bedggood and A. Metha, "Direct visualization and characterization of erythrocyte flow in human retinal capillaries," Biomed. Opt. Express **3**(12), 3264–3277 (2012).
24. A. de Castro, G. Huang, L. Sawides, T. Luo, and S. A. Burns, "Rapid high resolution imaging with a dual-channel scanning technique," Opt. Lett. **41**(8), 1881–1884 (2016).
25. A. Dubra, Z. Harvey, B. Fischer, B. M. Dawant, and C. Lorenz, "Registration of 2D Images from Fast Scanning Ophthalmic Instruments," in *Biomedical Image Registration*, Lecture Notes in Computer Science No. 6204 (Springer Berlin Heidelberg, 1), pp. 60–71.
26. J. A. Martin and A. Roorda, "Pulsatility of Parafoveal Capillary Leukocytes," Exp. Eye Res. **88**(3), 356–360 (2009).
27. C. E. Riva, S. Harino, R. D. Shonat, and B. L. Petrig, "Flicker evoked increase in optic nerve head blood flow in anesthetized cats," Neurosci. Lett. **128**(2), 291–296 (1991).
28. C. E. Riva, E. Logean, and B. Falsini, "Visually evoked hemodynamical response and assessment of neurovascular coupling in the optic nerve and retina," Prog. Retin. Eye Res. **24**(2), 183–215 (2005).
29. J. Schallek, H. Li, R. Kardon, Y. Kwon, M. Abramoff, P. Soliz, and D. Ts'o, "Stimulus-Evoked Intrinsic Optical Signals in the Retina: Spatial and Temporal Characteristics," Invest. Ophthalmol. Vis. Sci. **50**(10), 4865–4872 (2009).
30. J. Schallek and D. Ts'o, "Blood Contrast Agents Enhance Intrinsic Signals in the Retina: Evidence for an Underlying Blood Volume Component," Invest. Ophthalmol. Vis. Sci. **52**(3), 1325–1335 (2011).
31. Z. Zhong, G. Huang, T. Y. P. Chui, B. L. Petrig, and S. A. Burns, "Local flicker stimulation evokes local retinal blood velocity changes," J. Vis. **12**(6), 3 (2012).
32. M. J. Dumskyj, J. E. Eriksen, C. J. Doré, and E. M. Kohner, "Autoregulation in the Human Retinal Circulation: Assessment Using Isometric Exercise, Laser Doppler Velocimetry, and Computer-Assisted Image Analysis," Microvasc. Res. **51**(3), 378–392 (1996).
33. Y. Zhang, O. San Emeterio Nateras, Q. Peng, C. A. Rosende, and T. Q. Duong, "Blood Flow MRI of the Human Retina/Choroid During Rest and Isometric Exercise," Invest. Ophthalmol. Vis. Sci. **53**(7), 4299–4305 (2012).
34. T. J. H. Essex and P. O. Byrne, "A laser Doppler scanner for imaging blood flow in skin," J. Biomed. Eng. **13**(3), 189–194 (1991).
35. B. R. Berg and I. H. Sarelius, "Erythrocyte flux in capillary networks during maturation: implications for oxygen delivery," Am. J. Physiol. **271**(6 Pt 2), H2263–H2273 (1996).
36. ANSI, "American National Standard for Safe Use of Lasers," ANSI Z136.1 (2014).
37. G. Wyszecki and W. S. Stiles, *Color Science: Concepts and Methods, Quantitative Data E Formulae* (Wiley, 2000).
38. G. Wald, "Human Vision and the Spectrum," Science **101**(2635), 653–658 (1945).
39. Y. Geng, A. Dubra, L. Yin, W. H. Merigan, R. Sharma, R. T. Libby, and D. R. Williams, "Adaptive optics retinal imaging in the living mouse eye," Biomed. Opt. Express **3**(4), 715–734 (2012).
40. A. Guevara-Torres, D. R. Williams, and J. B. Schallek, "Imaging translucent cell bodies in the living mouse retina without contrast agents," Biomed. Opt. Express **6**(6), 2106–2119 (2015).
41. D. Scoles, Y. N. Sulai, C. S. Langlo, G. A. Fishman, C. A. Curcio, J. Carroll, and A. Dubra, "*In Vivo* Imaging of Human Cone Photoreceptor Inner Segments," Invest. Ophthalmol. Vis. Sci. **55**(7), 4244–4251 (2014).

Biomedical Optics EXPRESS

42. T. Y. P. Chui, D. A. Vannasdale, and S. A. Burns, "The use of forward scatter to improve retinal vascular imaging with an adaptive optics scanning laser ophthalmoscope," Biomed. Opt. Express **3**(10), 2537–2549 (2012).
43. A. Dubra and Z. Harvey, "Registration of 2D Images from Fast Scanning Ophthalmic Instruments," in *Biomedical Image Registration*, Lecture Notes in Computer Science (Springer Berlin / Heidelberg, 2010), Vol. 6204, pp. 60–71–71.
44. J. Tam, J. A. Martin, and A. Roorda, "Noninvasive Visualization and Analysis of Parafoveal Capillaries in Humans," Invest. Ophthalmol. Vis. Sci. **51**(3), 1691–1698 (2010).
45. S. Remtulla and P. E. Hallett, "A schematic eye for the mouse, and comparisons with the rat," Vision Res. **25**(1), 21–31 (1985).
46. C. Schmucker and F. Schaeffel, "A paraxial schematic eye model for the growing C57BL/6 mouse," Vision Res. **44**(16), 1857–1867 (2004).
47. The Jackson Laboratory: Mouse phenome database at the Jackson Laboratory, "Physiological Data Summary – C57BL/6J (000664)," (2007).
48. R. M. Hochmuth, R. N. Marple, and S. P. Sutera, "Capillary blood flow. I. Erythrocyte deformation in glass capillaries," Microvasc. Res. **2**(4), 409–419 (1970).
49. J. Schallek, Y. Geng, H. Nguyen, and D. R. Williams, "Morphology and Topography of Retinal Pericytes in the Living Mouse Retina Using *In Vivo* Adaptive Optics Imaging and *Ex Vivo* Characterization," Invest. Ophthalmol. Vis. Sci. **54**(13), 8237–8250 (2013).
50. H. Vink and B. R. Duling, "Identification of Distinct Luminal Domains for Macromolecules, Erythrocytes, and Leukocytes Within Mammalian Capillaries," Circ. Res. **79**(3), 581–589 (1996).
51. R. Skalak and P. I. Branemark, "Deformation of Red Blood Cells in Capillaries," Science **164**(3880), 717–719 (1969).
52. J. H. Jeong, Y. Sugii, M. Minamiyama, and K. Okamoto, "Measurement of RBC deformation and velocity in capillaries *in vivo*," Microvasc. Res. **71**(3), 212–217 (2006).
53. K. Y. Li and A. Roorda, "Automated identification of cone photoreceptors in adaptive optics retinal images," J. Opt. Soc. Am. A **24**(5), 1358–1363 (2007).
54. J. L. McWhirter, H. Noguchi, and G. Gompper, "Flow-induced clustering and alignment of vesicles and red blood cells in microcapillaries," Proc. Natl. Acad. Sci. U.S.A. **106**(15), 6039–6043 (2009).
55. M. Paques, R. Tadayoni, R. Sercombe, P. Laurent, O. Genevois, A. Gaudric, and E. Vicaut, "Structural and Hemodynamic Analysis of the Mouse Retinal Microcirculation," Invest. Ophthalmol. Vis. Sci. **44**(11), 4960–4967 (2003).
56. N. E. Everds, "Chapter 5 - Hematology of the Laboratory Mouse A2," in *The Mouse in Biomedical Research,* 2nd ed., M. T. Davisson, F. W. Quimby, S. W. Barthold, C. E. Newcomer, and A. L. Smith, eds. (Academic Press, 2007), pp. 133–153.
57. T. E. Kornfield and E. A. Newman, "Regulation of Blood Flow in the Retinal Trilaminar Vascular Network," J. Neurosci. **34**(34), 11504–11513 (2014).
58. L. Sargento, H. Sobral do Rosário, C. Saldanha, and J. Martins-Silva, "Hemorheological effects of sodium fluorescein in rats," Clin. Hemorheol. Microcirc. **24**(3), 175–181 (2001).
59. S. P. Sutera, V. Seshadri, P. A. Croce, and R. M. Hochmuth, "Capillary blood flow. II. Deformable model cells in tube flow," Microvasc. Res. **2**(4), 420–433 (1970).
60. A. R. Pries, T. W. Secomb, P. Gaehtgens, and J. F. Gross, "Blood flow in microvascular networks. Experiments and simulation," Circ. Res. **67**(4), 826–834 (1990).
61. A. Parpaleix, Y. Goulam Houssen, and S. Charpak, "Imaging local neuronal activity by monitoring PO_2 transients in capillaries," Nat. Med. **19**(2), 241–246 (2013).
62. J. Lecoq, A. Parpaleix, E. Roussakis, M. Ducros, Y. Goulam Houssen, S. A. Vinogradov, and S. Charpak, "Simultaneous two-photon imaging of oxygen and blood flow in deep cerebral vessels," Nat. Med. **17**(7), 893–898 (2011).
63. J. Perkkiö and R. Keskinen, "Hematocrit reduction in bifurcations due to plasma skimming," Bull. Math. Biol. **45**(1), 41–50 (1983).
64. K. H. Albrecht, P. Gaehtgens, A. Pries, and M. Heuser, "The Fahraeus effect in narrow capillaries (i.d. 3.3 to 11.0 µm)," Microvasc. Res. **18**(1), 33–47 (1979).
65. F. Felberer, M. Rechenmacher, R. Haindl, B. Baumann, C. K. Hitzenberger, and M. Pircher, "Imaging of retinal vasculature using adaptive optics SLO/OCT," Biomed. Opt. Express **6**(4), 1407–1418 (2015).
66. R. J. Zawadzki, P. Zhang, A. Zam, E. B. Miller, M. Goswami, X. Wang, R. S. Jonnal, S.-H. Lee, D. Y. Kim, J. G. Flannery, J. S. Werner, M. E. Burns, and E. N. Pugh, Jr., "Adaptive-optics SLO imaging combined with widefield OCT and SLO enables precise 3D localization of fluorescent cells in the mouse retina," Biomed. Opt. Express **6**(6), 2191–2210 (2015).
67. T. E. de Carlo, A. Romano, N. K. Waheed, and J. S. Duker, "A review of optical coherence tomography angiography (OCTA)," International Journal of Retina and Vitreous **1**(1), 5 (2015).
68. C. Riva, B. Ross, and G. B. Benedek, "Laser Doppler Measurements of Blood Flow in Capillary Tubes and Retinal Arteries," Invest. Ophthalmol. **11**(11), 936–944 (1972).
69. R. A. Leitgeb, R. M. Werkmeister, C. Blatter, and L. Schmetterer, "Doppler Optical Coherence Tomography," Prog. Retin. Eye Res. **41**, 26–43 (2014).

Biomedical Optics EXPRESS

70. D. A. Boas and A. K. Dunn, "Laser speckle contrast imaging in biomedical optics," J. Biomed. Opt. **15**, 11109 (2010).
71. T. Sugiyama, M. Araie, C. E. Riva, L. Schmetterer, and S. Orgul, "Use of laser speckle flowgraphy in ocular blood flow research," Acta Ophthalmol. **88**(7), 723–729 (2010).
72. B. Li, J. Lee, D. A. Boas, and F. Lesage, "Contribution of low- and high-flux capillaries to slow hemodynamic fluctuations in the cerebral cortex of mice," J. Cereb. Blood Flow Metab. **36**(8), 1351–1356 (2016).
73. Y. Jia, J. C. Morrison, J. Tokayer, O. Tan, L. Lombardi, B. Baumann, C. D. Lu, W. Choi, J. G. Fujimoto, and D. Huang, "Quantitative OCT angiography of optic nerve head blood flow," Biomed. Opt. Express **3**(12), 3127–3137 (2012).
74. C.-L. Chen, A. Zhang, K. D. Bojikian, J. C. Wen, Q. Zhang, C. Xin, R. C. Mudumbai, M. A. Johnstone, P. P. Chen, and R. K. Wang, "Peripapillary Retinal Nerve Fiber Layer Vascular Microcirculation in Glaucoma Using Optical Coherence Tomography-Based Microangiography," Invest. Ophthalmol. Vis. Sci. **57**(9), OCT475 (2016).
75. Y. N. Sulai, D. Scoles, Z. Harvey, and A. Dubra, "Visualization of retinal vascular structure and perfusion with a nonconfocal adaptive optics scanning light ophthalmoscope," J. Opt. Soc. Am. A **31**(3), 569–579 (2014).
76. Q. Yang, J. Zhang, K. Nozato, K. Saito, D. R. Williams, A. Roorda, and E. A. Rossi, "Closed-loop optical stabilization and digital image registration in adaptive optics scanning light ophthalmoscopy," Biomed. Opt. Express **5**(9), 3174–3191 (2014).
77. J. Zhang, Q. Yang, K. Saito, K. Nozato, D. R. Williams, and E. A. Rossi, "An adaptive optics imaging system designed for clinical use," Biomed. Opt. Express **6**(6), 2120–2137 (2015).

1. Introduction

The delivery of metabolites and removal of waste products at the tissue level is largely mediated by capillary perfusion. Within single capillaries, the exchange of oxygen and metabolic byproducts is provided by the passage of red blood cells (RBCs) that compress and flow in single file through vessels as small as ~4 micrometers in diameter [1]. This design maximizes surface area and optimizes exchange, yet also makes the capillary network fragile and susceptible to vascular disease. In the retinal circulation, a balance must be struck as the capillary network must both maintain the integrity of the blood-retinal barrier and enable metabolite diffusivity to feed retinal neurons, which have exceptionally high metabolic activity [2,3]. Dysfunction of this network is seen in a variety of retinal vascular diseases that collectively give rise to the leading causes of blindness in the developed world [4–8]. Many of these diseases, like diabetic retinopathy, are believed to originate first with capillary-level changes [9,10]. While the study of single blood cell hemodynamics has been performed in a variety of living tissues [11–15], many of these approaches are invasive and limited to experimental investigation or superficial tissues. Conversely, the eye provides a clear optical window through which central nervous system blood flow can be studied non-invasively. Unfortunately, the study of retinal capillary hemodynamics has been challenging due to several technical limitations. A major challenge has been achieving sufficient optical resolution to visualize single capillaries and the blood cells within. The imperfect optics of the mammalian anterior eye induce aberrations that blur the microscopic features of the retina [16,17]. As such, the spatial resolution of conventional retinal imaging approaches is typically 10-13 μm when correcting for defocus alone [17]. This resolution is insufficient to visualize single blood cells, which are ~6.5 μm in diameter and are further compressed as they flow within capillaries that are of smaller diameter [18]. To mitigate optical blur, the advent of adaptive optics ophthalmoscopy has enabled diffraction-limited imaging of the retina by measuring and correcting for high and low order aberrations of the eye [16]. Using adaptive optics correction, several groups have provided velocity measurements in retinal capillaries, arterioles and venules [19–24]. Building on this work, detailed imaging of single blood cells and their hemodynamic rheology could provide further information on microvascular flow and its disruption in retinal disease.

Blood cell imaging in the retina has been difficult not only because cells are microscopic, but also because they are constantly in motion. Image registration and frame averaging approaches [25] cannot be applied because blood cell position changes from frame to frame. Imaging blood cells requires high frame rate cameras to mitigate "motion-blur". Bedggood and Metha demonstrated that by using short epochs of data capture (~130 ms) with cMOS

Biomedical Optics EXPRESS

camera operating at 460 fps, they could image blood cells in motion to generate micro-sequences of capillary blood flow [23]. However, due to visible light exposure constraints, repeat testing beyond a handful of short epochs could not be performed until days later. This limits the study of perfusion to a snapshot in time, and therefore could not be used to study of the impact of the cardiac cycle [20,26], visually evoked stimulation [27–31], or other systemic changes that happen on longer time scales [32,33].

Unfortunately, fast cameras require even more light to provide sufficient detector exposure. This is especially problematic in the retina because imaging light must be at low power to avoid damaging the light sensitive tissue. This constrains the available signal-to-noise that can be produced in a single short-exposure frame. The ANSI limit for light exposure to the retina is strict, whereas other tissues that may be imaged, such as skin [34], superficial muscle [35] and the brain [11], may use more light intensity due to relaxed phototoxicity standards [36]. Making matters worse, 420-590 nm light, which optimizes hemoglobin contrast in red blood cells, is also more phototoxic to the retina and overlaps substantially with the spectra of maximum retinal photosensitivity, V_λ [37,38].

Collectively, these technical constraints have provided a formidable challenge to non-invasively image single blood cell hemodynamics throughout the early natural history of retinal microvascular disease. To surmount these limitations, we have developed an approach that combines adaptive optics ophthalmoscopy to overcome aberrations and fast data capture to mitigate motion-blur. Additionally, we have optimized contrast in single blood cells by using low power near infrared light and split-detector imaging to reveal the details of blood cells.

Deploying the above strategies in the mouse eye, we position a fast 15.45 kHz point scan orthogonal to a capillary of interest and image single blood cells as they pass the stationary scanning beam. To our knowledge, we report for the first time the ability to count blood cell flux with single cell accuracy, measure blood cell deformation, determine capillary level hematocrit, image blood cell rheology and compute instantaneous cell velocity of passing blood cells in retinal capillaries without using contrast agents.

2. Methods

2.1 Mouse preparation

C57BL/6J mice (Jackson Labs original stock 000664, Bar Harbor Maine) were imaged in this study. Mice were anesthetized with an initial intraperitoneal injection of ketamine/xylazine (100 mg/kg ketamine, 10 mg/kg xylazine) followed by the use of isoflurane at 0.5-1% delivered with supplemental oxygen to maintain anesthesia. Pupils were dilated using topical 1% tropicamide (Sandoz, Basel, Switzerland) and 2% phenylephrine (Akorn, Lake Forest, Illinois). During the imaging session, the mouse was placed into a stereotactic stage that allowed 5-degrees of freedom to microposition the mouse and align the mouse pupil. An X,Y, and Z positioning stage was used to align the pupil, and a two-axis rotation stage was used to navigate the imaging field to different retinal locations. The hydration of the cornea was maintained with a 1.6mm base curve contact lens with 0 to + 10D correction (Advanced Vision Technologies, Lakewood, Colorado). Body temperature was maintained with a supplemental heat pad and-or a feedback loop to maintain a systemic temperature of 37°C. Typical imaging sessions lasted between 30 minutes to 2 hours, after which the animals were allowed to recover and were returned to their cage for use in subsequent experiments.

2.2 AOSLO system

The mouse Adaptive Optics Scanning Light Ophthalmoscope (AOSLO) has been described in detail in previous publications [39,40]. It is a scanning imaging system composed of 5 pairs of afocal telescopes that relay coaligned beams for imaging and wavefront sensing. In the return path, light is reflected into high sensitivity photomultiplier tubes (Fig. 1). The eye aberrations

Biomedical Optics EXPRESS

were measured in real time with a Shack-Hartmann wavefront sensor using either an 843nm or 904 nm laser source (QPhotonics, Ann Arbor, Michigan). High and low order aberrations of the mouse eye were corrected with a deformable mirror that provided high-stroke compensation (ALPAO, Montbonnot-Saint-Martin, France). The near-infrared imaging source for this investigation was a super luminescent diode (central wavelength 796 nm, spectral width 17 nm, SUPERLUM, Ireland), and no fluorescent labels were required to capture blood cell images. The scanning system collected 2-dimensional raster images at a rate of 25 frames per second, with 1-D fast scanning operating at 15.45kHz.

For validation, we also injected sodium fluorescein in a small subset of experiments to image labeled blood plasma. An intraperitoneal injection of 0.1 mL of sodium fluorescein (2.5% w/v AK-FLUOR, Akorn, Inc.) was administered. Fluorescence was excited with 488nm laser (~50-70 μW) from a Toptica multi laser engine (MLE-L, Toptica, Victor, NY, USA). Simultaneous fluorescence imaging was performed in a third PMT, capturing fluorescence with a 520/35 nm emission filter.

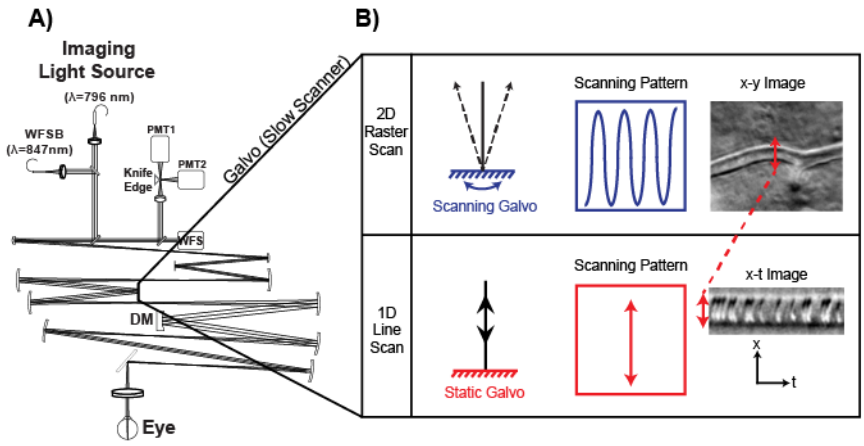

Fig. 1. A) Optical setup of the non-confocal AOSLO. This system uses a 796nm superluminescent diode for imaging and a 847nm (or 904nm) laser as the wavefront sensing beacon (WFSB). In place of a typical confocal pinhole, a knife edge beamsplitter splits light into two detectors with synchronized acquisition. B) The two scanning modes. The 2D raster scan captured en-face images of the retina. The other scanning pattern was "line scan", where the 15.45 kHz resonance scanner scanned a point orthogonally to the capillary of interest. RBCs were imaged as they moved across the stationary imaging beam. This imaging scheme yields images where the ordinate axis is space and the abscissa represents time. A third visible light source and synchronized detector (not shown) were used for sodium fluorescein excitation/imaging.

2.3 Split-detector imaging

Split-detector imaging was performed in a convention described previously [40,41]. Briefly, the imaging system projected a diffraction-limited spot onto the retina to generate a raster image. The spot in the retina was then descanned and reimaged into a detection plane. The retinal point spread function (PSF) was bisected by a knife-edge prism oriented orthogonally to the direction of the fast resonance scanner, (x-axis Fig. 1) [40]. Light from left and right-half of the imaged PSF was detected by two photomultiplier tubes (PMTs) (H7422 –50, Hamamatsu Corporation, Shizuoka-Ken, Japan) with synchronized acquisition. The subtraction between the two channels served to cancel common information in the two images and enhanced the residual difference. Differential contrast is believed to be a product of the multiply scattered light in non-confocal detection [42].

Biomedical Optics EXPRESS

For comparison purposes, a small subset of the data was collected with the system in confocal configuration using the near infrared channel (796 nm). This was performed by substituting the knife edge with a confocal aperture of 50μm (2.1 Airy disc diameters) at the plane of optimal focus in front of the PMTs.

2.4 2D image capture, sinusoidal scanner correction and image registration

In the 2D image modality, en face images were captured by scanning across the region of interest (Fig. 1(B), top). The layer of interest was selected by applying a fine defocus control to the deformable mirror. Field sizes of either 5 deg, 2 deg or 0.5 deg were selected by controlling the voltage amplitudes of the scanners. Sinusoidal distortion of the resonance scanner was digitally corrected using a Ronchi ruling as calibration. Multiple frames were captured at a rate of 25Hz, and the global motion due to respiratory and cardiac activity was digitally registered with post-processing strategies similar to those reported by Dubra and Harvey [43]. The field motion was estimated using the cross correlations to a reference frame using only spatial frequencies within the diffraction limit of the system. The final split-detector images were obtained by averaging the registered frames, giving a high signal to noise ratio image.

2.5 Motion contrast images

To optimize contrast of blood vessels without injecting contrast agents, we computed the local "motion contrast" in the registered-stabilized video sequences. In this paradigm, the movement of blood cells causes the intensity of spatially registered pixels to vary over time. We calculated the motion contrast by computing pixel intensity standard deviation over time [44]. This approach provides positive contrast of locally dynamic features and suppresses static features in the image. Bright pixels in motion contrast images report high pixel variance induced by blood cell motion.

2.6 1D line scan imaging

To improve our ability to image RBCs, we increased the acquisition rate by scanning across a line perpendicular to a capillary of interest with a one-dimensional point-scan at a rate of 15.45 KHz as shown in Fig. 1(B) (lower panel) [20,21]. As the scanned line was stationary, the passage of the RBCs through the scanning region was captured over time. After the series of line scans were acquired, we first corrected for the sinusoidal distortion of the fast scanner and then calculated the difference between the two channels. When setting the scanner width to less than a degree of visual angle, the data is heavily oversampled both in the spatial and temporal dimensions. This allows spatial/temporal filters to bin the data, further increasing the signal to noise ratio.

The field size for the 1D line scan imaging sequence was 0.67 degrees, which corresponds to ~23μm in the spatial dimension [45,46]. The resolution limit of our system using 796nm light is 1μm, and this distance is sampled by 28 pixels. This means that the spatial information was oversampled by a factor of 14, considering the Nyquist limit. We therefore applied a conservative spatial Gaussian filter with a sigma of 7.5 pixels in digital post-processing. For symmetry, this same filter was applied in the temporal dimension without temporal sampling consequence. Using this strategy at 15.45 kHz line acquisition rate, the instrument can detect cells that are traveling up to 13 mm/s in retinal capillaries. This exceeds the known velocities of cells flowing though these retinal capillaries [22–24]. Data from a single capillary could be collected for minutes at a time without interruption. Contiguous capture was only limited by hard drive space. For the study of RBC flux and diameter over a population of 99 capillaries, we captured line scan sequences for 20 seconds. All images (1D and 2D) in this publication have been rotated by 90 degrees in the counter clockwise direction for display purposes. Space-time images plot space along the ordinate, and time along the abscissa.

Biomedical Optics EXPRESS

2.7 Measurement of cell flux

Blood cells imaged in line scan acquisition were manually counted by expert graders. The data is represented in a fixed aspect ratio that allows users to visualize blood cells in space-time images. Graders manually identified the center of each imaged cell with a unique space and time coordinate. For this task, we used the CellCounter plugin of ImageJ (National Institutes of Health). In this study, data from the first second of capture was analyzed to report mean flux. This approach averages temporal variation in blood cell flux over multiple cardiac cycles. In this study, all cells that filled the capillary lumen were assumed to be RBCs. White blood cells were also counted in the flux measurement, yet are not expected to appreciably skew RBC measurements as the ratio of red to white blood cells is 3400:1 in the mouse [47]. This means that total blood cell flux measurement only differs from true RBC flux by an error of 0.029%.

To study the influence of cardiac pulsatility, two 78.7 second line scan images were captured and RBCs were manually determined by two masked graders as described above. Capillaries were selected based on exemplary contrast, but differed in their flux and velocity content. Data was masked and compared across graders.

2.8 Measurement of hematocrit and cell velocity

To measure capillary hematocrit (volume fraction of RBCs with respect to the total blood volume), blood cell boundaries and the area occupied by capillary lumen in line scan images were manually segmented by an expert grader. Capillary hematocrit was calculated as the fraction of the area occupied by the RBCs relative to the area occupied by the capillary within the vessel, assuming steady flow.

To measure blood velocity, the centroids of RBCs were first manually marked by expert graders. The average cell was obtained using the unique x-t coordinates from each identified cell and then registering and averaging a fixed window of data surrounding the center position of each cell. Resultant average cell images show the registered summation of all marked RBCs relative to their identified centroid. In addition, the temporal width was calculated by first plotting the 1D profile of the cell along the time dimension by selecting the line that passes through the brightest pixel of the average cell image. This 1D profile has a central peak and the associated temporal width Δt is calculated as the full width at half maximum. Considering that each cell may have a unique velocity, the average cell analysis makes quick determination of average capillary blood speed. The velocity v, is calculated by the following equation:

$$v = \frac{d}{\Delta t} \tag{1}$$

where d is the length of the RBCs along the direction of flow. To assume a size for d, we take advantage of the homogeneity of RBC size that is physiologically bounded. Previous *ex vivo* studies have found that the deformation ratio of RBCs in glass capillaries of similar size range from 2.03 to 2.77 [48], taking into account a plasma layer of ~0.5 µm. Thus, in a capillary of diameter 3.6 µm, the parameter d lies between 7.3 – 10 µm. In all velocities reported in this work for capillaries of similar size, we will use the above specified range of deformation ratios.

2.9 Capillary lumen diameter measurement

The inner lumen diameter of capillaries was measured using a semi-automated approach. Residual motion in the spatial dimension of 1D line scan images was corrected with custom software in MATLAB (version 8.5.0 R2015a, MathWorks, Inc., Natick, Massachusetts). For each capillary, a region with one RBC surrounded by plasma was chosen as a reference image for spatial motion correction. The reference images had a temporal width ranging from 2 to 27

Biomedical Optics EXPRESS

ms: this variation accounts for the large range in blood cell speeds and local hematocrit. Normalized cross correlation was used to identify the 10 best correlated target images in 1 second of data capture. The 10 target images were spatially registered and then concatenated into a single contiguous strip. Average intensity over time showed the profile of the vessel. The variance in intensity over time showed the varying contrast from passing blood cells (standard deviation). (Fig. 2) The lumen diameter was measured to be the distance between the half-maximum crossings of the two prominent peaks of the standard deviation profile (appearance of double peak described in results). This criterion of luminal boundary also matched well with lumen diameters measured in different experiments using sodium fluorescein to determine the plasma-endothelium interface (not shown). Measured diameters were corrected for the relative angle between the 1D scan and the cross section of the capillary, which was not always precisely orthogonal. The average applied correction was 5% of the measured diameter, with the maximum correction ever applied being 23%. In capillaries, the lumen diameter we report is that of the central column of moving RBCs and does not include the thickness of the capillary wall comprised of endothelial cells and pericytes [49]. This measurement does not report or measure the thickness of the endothelium glycocalyx that is as much as ~0.5 microns thick [50], which would require nanometer-level resolution to be accurately distinguished.

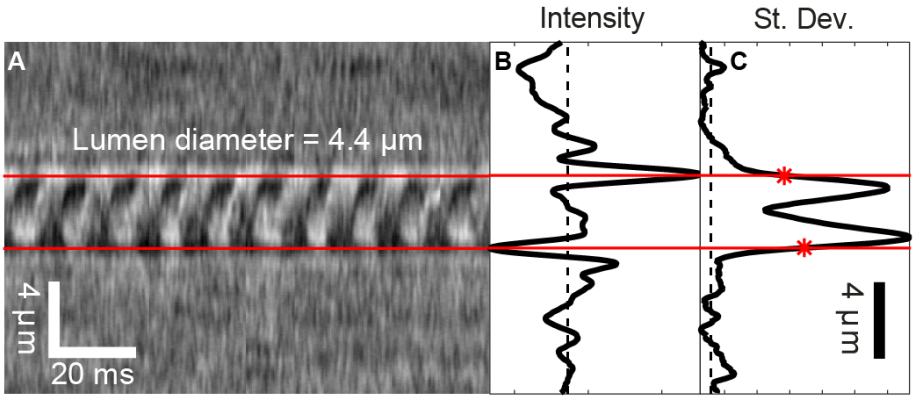

Fig. 2. A) Capillary lumen diameter measurement line scan image showing the 10 best correlated target images with respect to a user-selected reference image of RBC surrounded by plasma. B) Spatial intensity profile averaged over time. C) Standard deviation (St. Dev.) of pixel intensity across time. Dotted line in C shows mean standard deviation in regions clearly outside the lumen of the vessel.

3. Results

This approach reveals a new set of measurements and biomarkers that quantify vascular flow in the retina at the level of capillaries. Measurements were obtained from 10 mice and this strategy showed successful imaging of blood cells in all mice. Using these images, we measured capillary width, RBC flux, arrangement, hematocrit and velocity.

3.1 Imaging static RBCs in-vivo

We observed short epochs where single blood cells became arrested within capillaries. In the 14 imaging sessions that involved the study of 99 capillaries, we observed only 1 instance of stopped blood flow. Stoppages lasted from seconds-to-minutes at a time. In one of these rare events, we took advantage of the static nature blood cells to average many frames to improve the signal to noise of the 2D imaging approach. In Fig. 3(A), we show the average of 850 frames (~34 seconds) where cells were stationary in a capillary (Visualization 1). In agreement with the known morphology of RBCs, images show the classic biconcavity of RBCs. We also see the deformation of blood cells that must compress in capillaries ~4

Biomedical Optics EXPRESS

microns in diameter. The deformation ratio of cells in this image is on average 2.23 (n = 4 long-to-short axis ratio), which is consistent with the ranges observed in other tissues [48,51,52]. This cell compression is similar to the one observed in mouse retinal microvessels imaged with bright-field microscopy (Olympus BX43) using post-mortem histology approaches (Fig. 3(B)). *In vivo* and *ex vivo* images are shown at the same scale and reveal similar morphometry of single red blood cells. Differential contrast arises from the curved surfaces of the biconcave RBCs.

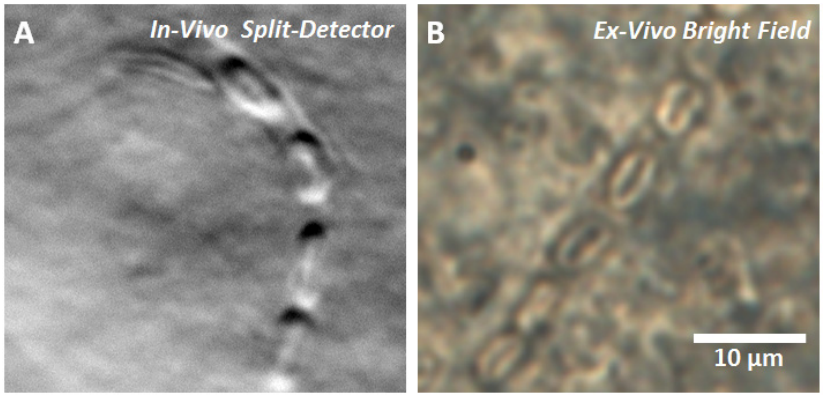

Fig. 3. A) Deformed RBCs observed in the living mouse eye imaged with split-detector configuration over 34 seconds of stopped flow (Visualization 1). B) Deformed RBCs as observed in the *ex vivo* retina of a different mouse using a 40x bright field microscope. The biconcavity of RBCs can be observed in both cases.

3.2 Imaging flowing blood cells with 1D line scan imaging

When 15.45 kHz line was positioned orthogonally to a capillary, the profiles of single blood cells were reconstructed over time as they passed the scanning line (Fig. 4). By counting the number of cells that cross the 1D scanning region, we can obtain a direct measure of RBC flux. When a confocal pinhole was placed in front of the detector, passing blood cells were seen as small glints, which poorly represented blood cell structure despite AOSLO resolution (Fig. 4(A), 4(B)). The split-detector approach revealed a significant increase in the contrast and visualization of cell morphology, size and deformation while using the equivalent levels of near infrared light (Fig. 4(D), 4(G)). Some cells appear longer than others in the time dimension, the temporal "length" of cells is indicative of cell speed. Slow moving cells will take longer to pass the beam and will appear longer in the images.

Sodium fluorescein labeling, in a subset of experiments, further confirmed blood cell detection. Single blood cells imaged using split-detection corresponded to a concurrent dip in intensity in the fluorescence imaging channel. This negative contrast is observed because plasma (and not blood cells) is strongly labeled with fluorescein (Fig. 4(E), 4(H)). In cases with fast moving RBCs and reduced RBC spacing (Fig. 4(G), 4(H)), we could reliably discern and count blood cells using split-detector, yet the contrast provided with sodium fluorescein was considerably weaker, leading to an apparent undercount of actual passing blood cells (Fig. 4(G), 4(H), central clusters). Using more imaging light was not possible without imparting photodamage of the retina [36].

Biomedical Optics EXPRESS

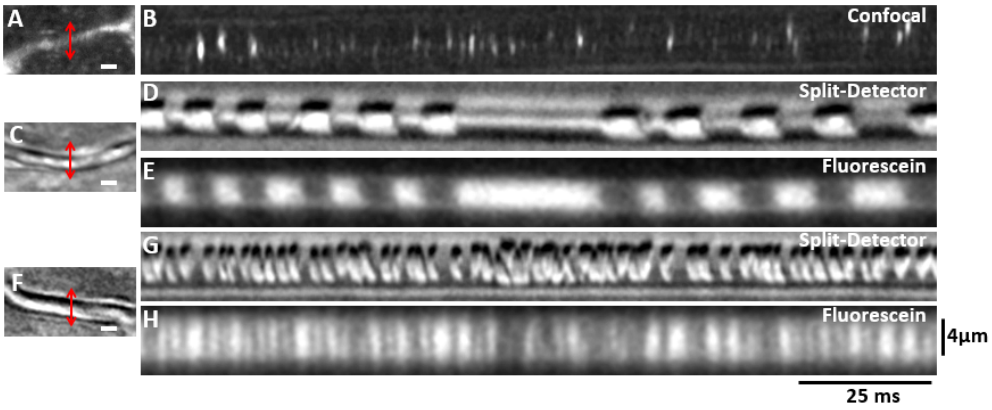

Fig. 4. A) 2D motion contrast image of a capillary in confocal configuration B) The corresponding confocal 1D line scan sequence revealing blood cell glints. C) 2D raster image of a capillary in a different animal captured in split configuration D) Corresponding line scan sequence. Split-detector reveals shape, deformation and arrangement of red blood cells. E) Simultaneously acquired line scan fluorescence from blood plasma labeled with sodium fluorescein. F) 2D raster image of a second blood vessel in the same animal containing high flux and G) corresponding split-detector line scan sequence. H) Simultaneously acquired plasma fluorescence. RBC flux is considerably higher in capillary F compared to C. In cases of high RBC flux and high capillary hematocrit, it is more challenging to distinguish individual RBCs in the fluorescence image compared to the contrast provided by split-detector. Scale bar for A, C and F: 4µm. Fluorescence images have been corrected for small lateral offsets in the time dimension (relative to split-detector images) due to transverse chromatic aberration.

3.3 Local capillary hematocrit is variable

The line-scan approach enabled measurement of the local capillary hematocrit (volume fraction of RBCs with respect to the total blood volume), which can be considerably different from systemic samples of whole blood hematocrit. Evidence of this range of capillary hematocrit was quantified in the two capillaries shown in Fig. 5(A) and 5(C). They both have a diameter of 3.5 µm and similar blood velocity (see section 2.8). Although the capillary in Fig. 5(A) had a slightly higher velocity than the capillary in 5C (2.34 vs. 1.96 mm/s), its flux was lower (77 vs 119 cells/s). This is due to capillary specific variations in local hematocrit: the capillary in Fig. 5(A) has a measured hematocrit of 0.24 (volume fraction of RBCs to the total blood volume), while capillary in Fig. 5(C) has a hematocrit of 0.43, nearly twice that of the first capillary.

3.4 Blood cell arrangement

The split-detector, line-scan configuration provided detailed images of the morphology and arrangement of flowing blood cells within the capillary network. The most common morphology observed was the parachute configuration (85% of capillaries, n = 99, Fig. 5(A), 5(C)), where cells are deformed by the pressure difference and the shear stress of the vessel wall [51]. This flow pattern was often found in straight vessels, and away from vessel branch points. We also observed RBCs arranging on a zigzag configuration where cells interdigitate (1% of capillaries, n = 99, Fig. 5(D)). The zigzag configuration was found near points of capillary confluence. There were other cases when cells did not have a consistent orientation or morphology (14% of capillaries, n = 99, Fig. 5(E)); these were considered to have a disordered flow [18].

Biomedical Optics EXPRESS

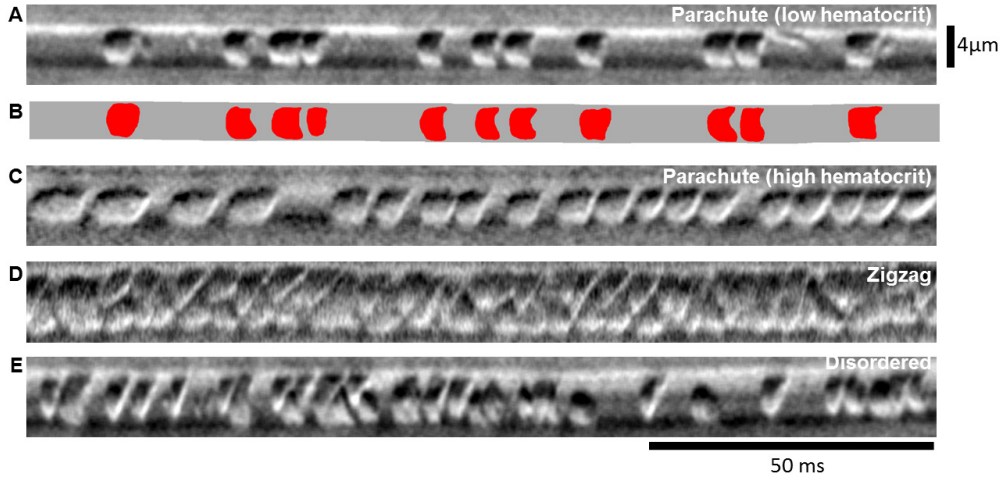

Fig. 5. RBCs arranged in different configurations as observed in four different retinal capillaries A) RBCs arranged in parachute configuration. B) Manual segmentation of the RBC boundaries in A are shown in red and capillary boundaries in gray. C) Capillary with similar blood velocity and diameter, but with higher volume fraction of RBCs (local hematocrit) D) RBCs arranged in a zigzag configuration where blood cells closely interdigitate with minimal plasma gaps. E) Capillary with disordered flow shows RBCs without consistent arrangement or orientation.

3.5 Computing the average RBC reveals average cell velocity and flow periodicity

We observed tens-to-hundreds of cells passing per second in capillaries. These numbers lend themselves to averaging strategies to report the dimensions of the "average blood cell". In addition to average cell width, we found two other metrics could be quantified. The first is an estimation of average RBC velocity. Based on the assumptions stated in section 2.8, we determine the cell velocity range for capillary 1 of Fig. 6 to be 0.45 to 0.61 mm/s. The dwell time of the average cell in capillary 2 of Fig. 6 was shorter because cells are moving faster. Average RBC velocity in this capillary is between 0.73 and 0.99 mm/s.

Computation of the average blood cell also revealed that some capillaries contained highly periodic flow patterns and produced average RBC images with the appearance of temporally flanking cells (Fig. 6(B)). These flanking cells represent the additive likelihood of a consistent time separation between upstream and downstream cells. The constructive contrast of flanking RBCs suggests a periodic and consistent time separation between cells (Fig. 6(A)-6(C)). Other capillaries had more random temporal patterns of blood cell flux. In these cases, the central registered cell showed additive contrast, but the randomness of temporally adjacent cells did not provide constructive summation to produce a strong flanking cell image (Fig. 6(D)-6(F)). Therefore, the strength of the flanking cells may provide an index measure of the periodicity or randomness of cell flux.

Biomedical Optics EXPRESS

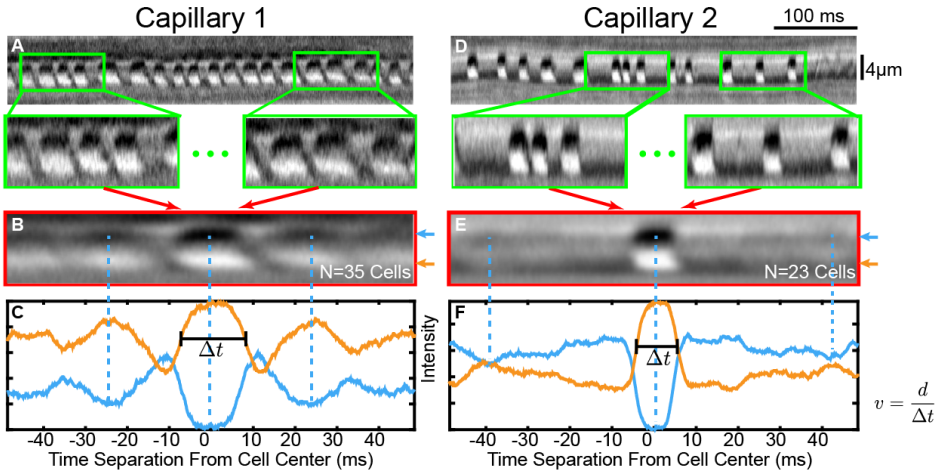

Fig. 6. A) Line scan image where a moving average window centered on each cell was used to generate its average cell. B) Average cell image corresponding to A where the average target cell is highly visible and because of the regularity in the flow, the average neighboring cells too have appreciable contrast. C) Plot of the pixel intensity of the two lines of the darkest and brightest pixels in the image also marked by the arrows on the right of B and E. The orange plot has a prominent central peak, where the width of the central peak is used to determine cell velocity. There are also slightly less prominent peaks on each side of the central one corresponding to the surrounding cells. D) Line scan image of another capillary with irregular spacing between cells E) Average cell plot corresponding to D where the average target cell is highly visible but because of the lack of regularity in flow, the average neighboring cells have washed out contrast due to temporal variability. F) Linear profile corresponding to the arrows on the right of E. The orange plot has very faint peaks on either side of the central peak.

3.6 Capillary pulsatility measured with instantaneous RBC flux

Line scan images captured for 78.7 seconds in two different capillaries were analyzed to study the influence of cardiac pulsatility. Analyzed vessels had a lumen diameter of ~3.6 μm, which represent true capillaries, and not arterioles or venules for example. Instantaneous RBC flux (the inverse of the time separation between cells), revealed a periodic modulation of RBC flux consistent with the heart rate of the anesthetized mouse (Fig. 7(A), only data for capillary with higher average flux shown). While the heart rate was not measured simultaneously with electrocardiography, we did find that the fast Fourier transform (FFT) produced a strong peak 176.9 cycles/min in the capillary, corresponding to the cardiac rate of the anesthetized mouse. RBC flux pulsatility was observed in each capillary regardless of total flux. Zooming into a subset of the data, we observe a periodic cycle indicative of the putative systolic and diastolic phase of the cardiac cycle (Fig. 7(B)). When the time separation between adjacent cells is large, the instantaneous flux is small. Additionally, the measured velocity of cells within the putative systolic and diastolic phases showed cells with faster and slower respective velocities (Fig. 7(B), right) indicating modulated rates of capillary blood flow.

To verify the pulsatility measurement, RBC identification was compared between two masked graders. FFT analysis for each user found the same frequency peak at 176.9 cycles/min. Not only were measurements of flux pulsatility consistent, but the overall agreement between users was >99.6% (Fig. 7(A)). Differences in total RBCs counted was 0.31% between two graders for the high flux capillary (grader 1 = 13770 cells, grader 2 = 13727 cells). In a second capillary with low flux, the difference in counts was 0.32% (grader 1 = 2843 cells, grader 2 = 2852 cells). This agreement is relatively high when compared to other manual cell detection approaches using adaptive optics images that are on the order of 1-9% difference between users [53]. The consistency in measurements suggests that blood

Biomedical Optics EXPRESS

cell contrast and identification is robust when captured in the split-detector, line scan modality.

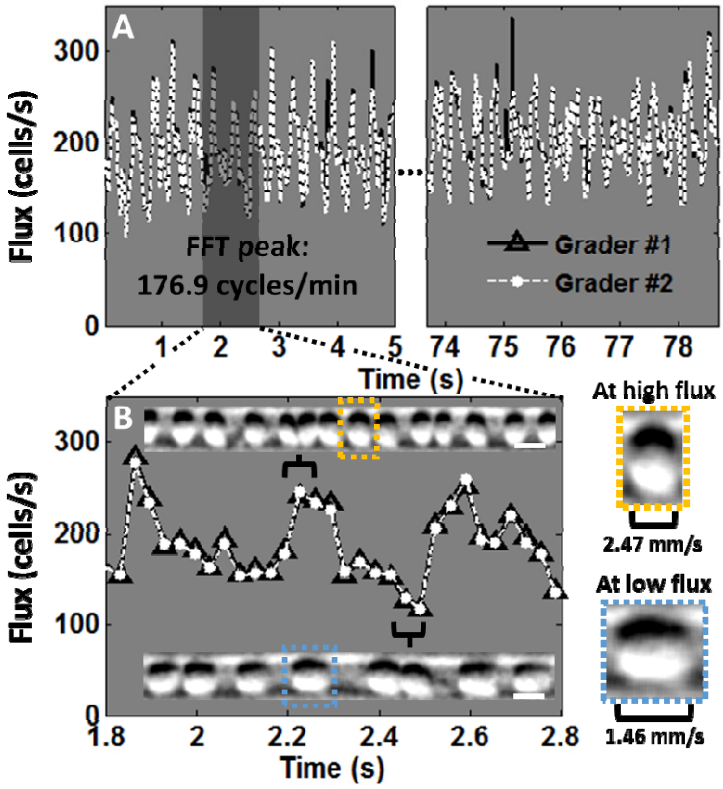

Fig. 7. A) Pulsatility of blood cell flux due to cardiac cycle is demonstrated in capillary with lumen diameter of 3.6 µm. Instantaneous flux is plotted over 78.7 seconds of continuous data capture. Only the first and last 5 seconds of measurements are shown for better visualization. The Fourier transform of measured flux showed a strong peak at 176.9 cycles/min (FFT not shown). For visualization, a moving average of 33 ms was applied to the raw data corresponding to an oversampling of 5.1x Nyquist limit of cell velocity. B) A zoomed region of instantaneous flux measured for 1 second of data (shaded region in A). Flux variability over time shows ~3 putative cardiac cycles. The arrangement of blood cells at the maximum and minimum of one cycle is shown inset (66 ms time windows, scale bar = 5 ms). Two representative RBCs in these time windows are magnified on the right. Using velocity estimation described in section 2.8, the representative RBC in the putative diastolic phase is ~41% slower as compared to that in the putative systolic epoch.

To rule out potential error induced by residual eye motion (e.g. movement of the stationary line scan beam relative to the capillary), we captured 2D raster images of the same capillaries shown in Fig. 7. The eye motion was computed using 2D cross correlation algorithm described in section 2.4. The maximum global eye motion was 21 µm/s. The blood velocity range of the data in Fig. 7 was between 1.46 and 2.47 mm/s. The maximum global motion of the eye is two orders of magnitude less than the measured velocity. The error induced by eye motion was calculated to be <2%. We therefore conclude that the pulsatile modulation in cell flux is a product of changes in cell flux and velocity due to cardiac cycle, and not an artifact of unstable positioning of the scanning beam on a single capillary.

3.7 Confluence of flow: parachute configuration interdigitates to zigzag configuration

In a region where two capillaries converge, we studied the confluence of flow and its impact on the flow patterns (Fig. 8). Blood flow direction was confirmed to be from left-to-right,

Biomedical Optics EXPRESS

therefore vessels B and E converge onto vessel D in Fig. 8. The parachute configuration was observed in upstream branches B and E. At the point of confluence (Fig. 8(C)) we visualized the interdigitation process of the converging branches. Further downstream, this interdigitated flow remained in the zigzag configuration 15 micrometers away from the point of confluence. Each of these flow patterns has been observed in other tissues. Some models suggest that these flow patterns are predicted by changes in velocity and local hematocrit [54]. Here we emphasize the importance of documenting the proximity of the flow pattern to the point of nearest vascular junction, which visibly imparts microturbulence of mixing multiple single-file streams.

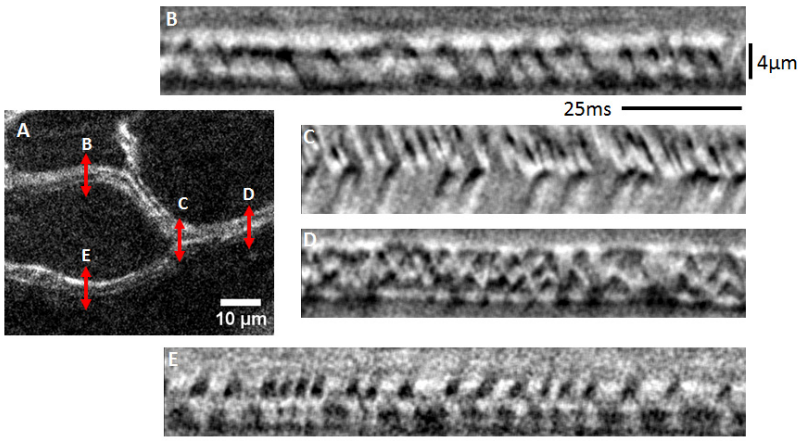

Fig. 8. A) Motion contrast image shows enhanced contrast of multiple converging capillaries in the living mouse retina. Line scans at positions indicated by arrows are compared in B-E. The convergence of vessels B and E containing parachute RBC flow become interdigitated at point of confluence (C) and remain in zigzag configuration 15 micrometers downstream.

3.8 Conservation of flux

To validate the accuracy of our flux quantification, we performed a test of flux conservation. In this test, we analyzed five capillary branches that formed a network of converging and diverging flow (Fig. 9). Our analysis revealed that flux was conserved; that is, the number of blood cells in an upstream branch equaled the counts of the connected downstream branches. For example, the convergence of branch 2 and branch 3 equaled the total flux observed in branch 1. The measured differences in conservation of flux were small, only showing error of 0.6% and 4.3% in the convergent branches of Fig. 9. Errors of this size were likely due to the sequential nature of capture, and tiny changes of total flux on the order of minutes. Without ground-truth values of actual blood cells, the conservation of flux analysis corroborates the robustness and accuracy of counts in single branches. Importantly, all branch points were accounted for in the en face image. Hidden anastomoses in the axial dimension were ruled out by looking for penetrating vessels when changing plane of focus.

Biomedical Optics EXPRESS

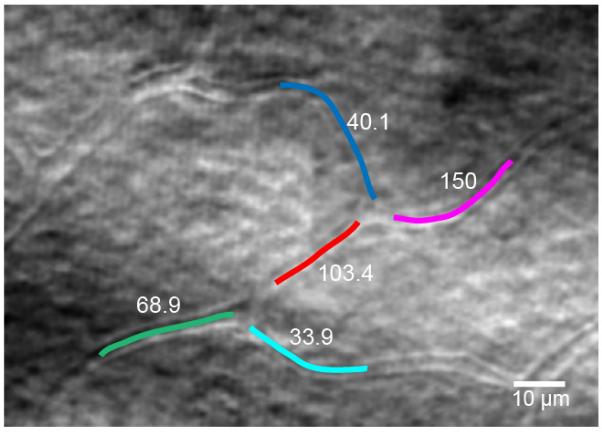

Measured Flux (RBCs/sec)				
Branch 1	Branch 2	Branch 3	Sum of 2+3	% Difference from 1
150	103.4	40.1	143.5	-4.3
103.4	68.9	33.9	102.8	-0.6

Fig. 9. Capillaries showing the conservation of flux. In both bifurcations we observe how the sum of the lower flux vessels is approximately equal to the one of the high flux vessel. There is a small difference in RBC flux of the different vessels, this is likely due to the sequential nature of capture and the variability contained therein.

3.9 Capillary RBC flux and lumen diameters in normal C57BL/6J mice

To determine the range of flux in the capillaries of the normal mouse retina, we performed manual counts of flux in 99 capillaries across 10 C57BL/6J mice from 13 to 37 weeks old. Our analysis was limited to vessels containing single file flow, and thus vessels >6.5 µm in diameter were not analyzed due to lateral cell stacking. Microvessels ≤6.5 µm showed a large distribution of cell flux ranging from 17 and 539 cells/sec, mean of 159 ± 11 cells/sec (± standard error of mean).

Flux counts were compared to lumen diameter for each of the 99 capillaries measured. Lumen diameters ranged from 3.2, to the upper bound of 6.5 µm, mean = 4.0 ± 0.7 µm (mean ± 1 standard deviation, N = 99 capillaries). 91% of capillaries in this population had a lumen diameter smaller than 5 µm and is commensurate with the size of the undeformed RBC in the mouse (~6.5 micrometers). The correlation between lumen diameter and flux was weak. An arbitrary fit of a linear correlation function shows R^2 = 0.24, (other polynomial, power and quadratic functions were similarly weak). The large spread of data and lack of strong correlation suggests capillary diameter alone is a weak predictor of total blood flux. This finding underscores the importance of objective flux measurement rather than modeling capillary flow based on diameter measurements alone. Evidence of the flux heterogeneity is shown in Fig. 10(B). Here, we show capillaries with similar lumen diameter can have visibly different RBC flux. Conversely, vessels with similar counts of flux may have considerably different lumen diameter.

Biomedical Optics EXPRESS

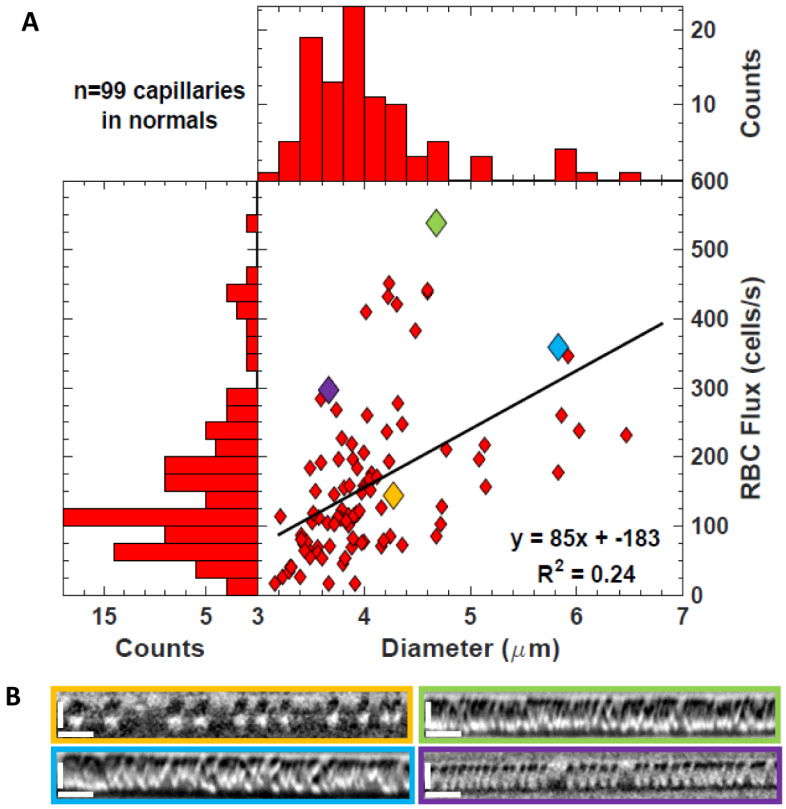

Fig. 10. A) Scatter plot of lumen diameters and RBC flux in 99 retinal capillaries across 10 animals, along with histograms of the distribution of flux and diameter. B) Sample line scan images from four capillaries. The colored boundary of each image corresponds to the same colored data point in the normal data set (A). Vertical scale bar is 4 μm and horizontal scale bar is 10 ms.

3.10 Despite lack of a confocal pinhole, split-detector imaging shows strong axial sectioning

In a conventional AOSLO, a confocal pinhole provides an increase in axial sectioning by rejecting out of focus light. In the split-detector configuration the lack of a pinhole may imply weak axial sectioning, however, we found the opposite. The split-detector configuration yielded high axial sectioning capabilities. By way of example, we were able to distinguish the three layers of vasculature in the mouse without overlap of adjacent vessel stratifications. The left column in Fig. 11 shows split-detector images of the three vascular layers imaged on the same retinal location, while the right column shows the corresponding motion contrast images. The independence of each of these vascular stratifications which are ~50 μm apart [55], demonstrate the axial resolution. In the mouse, this axial resolution is due to narrow depth of field; a product of a high numerical aperture (0.49 in the mouse [39]).

Biomedical Optics EXPRESS

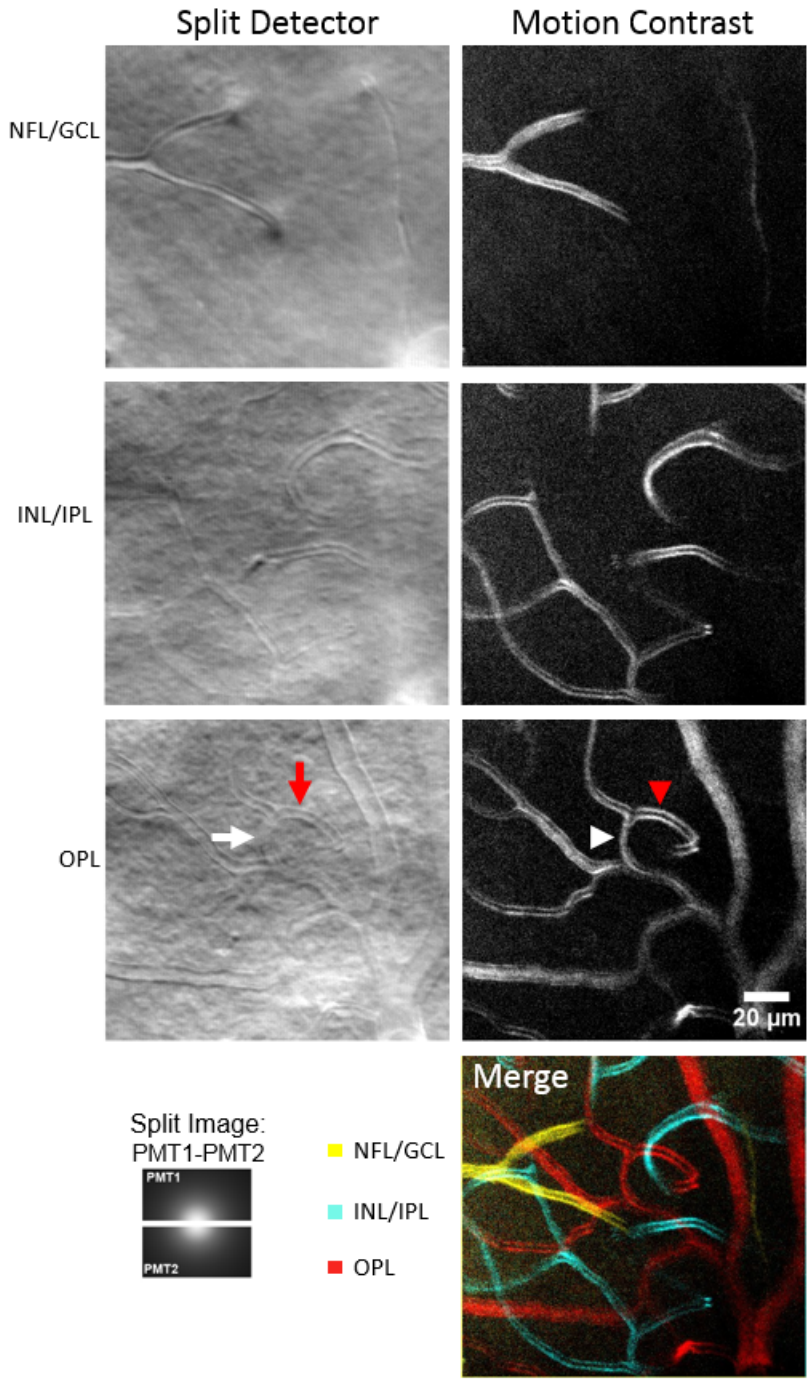

Fig. 11. Changing plane of focus provides independent imaging of the three vascular stratifications of the mouse retina. Split detector intensity images (left) and corresponding motion contrast images (right). Despite lack of a confocal pinhole, stratifications are independently imaged. Vessels parallel to the knife edge are most visible in the split–detector images (red arrow), whereas contrast from orthogonal vessels are less visible (white arrow). Motion contrast images show a double line profile in vessels parallel to the knife edge (red arrowhead) while a single line can be observed in orthogonal vessels (white arrowhead).

Biomedical Optics EXPRESS

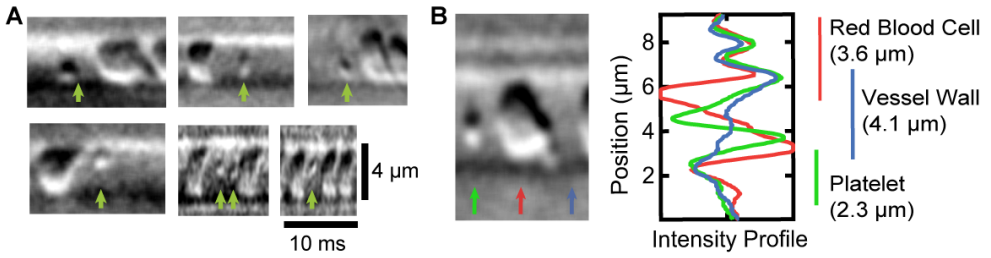

Fig. 12. A) Images of platelets visualized with line scan split-detector B) Enlarged image where an RBC, platelets and vessel wall can be clearly seen and the intensity profile of each of the vascular constituents is plotted to the right. The RBC and platelet have the same polarity of contrast (bright on top) while the vessel wall has the opposite polarity.

3.11 In-vivo platelet imaging

In addition to imaging RBCs, we also observed other components of blood far too small to be considered RBCs. In regions of large plasma gaps, we routinely observed small cells that did not fill the capillary lumen (Fig. 12). The main constituents of blood are RBCs, plasma, platelets and white blood cells. The size of the cells were generally between 1 and 3 μm, which is close to the known size of un-activated platelet population [56]. To show differences in cell size, the differences in profiles of the cell wall, RBC and single platelet are shown in Fig. 12(B). Manual counts of RBCs did not count this morphologically different cell class. We emphasize that cell counts provided in previous sections are not confused with identifying platelets. The resolution and contrast of split-detector AOSLO imaging allows us to differentiate these populations.

4. Discussion

The eye has long held the potential to serve as a window to study the central nervous system and its vascular network non-invasively. The retina is far more sensitive to ischemia than other peripheral tissues, as neural cells need an uninterrupted vascular supply. This workflow provides unique ways to study and characterize blood flow non-invasively. With this instrument, red blood cell flux, hematocrit, velocity, capillary width and cell arrangement may now be objectively quantified in the living eye. With these new metrics, we add to the available structural and functional biomarkers that may be studied in retinal disease.

4.1 Comparison to other label-required approaches to measure flux

To measure blood cell flux in the rodent eye, recent studies have injected fluorescent agents into the blood stream to measure gaps in fluorescent plasma (or labeled erythrocytes) and determine the number of passing blood cells in the retina [12,57]. This approach was among the first to quantify erythrocyte flux at the level of single capillaries; yet, there are remaining questions as to whether fluorescent labeling alters the viscosity, deformability or rheology of normal circulating blood cells [58]. Moreover, in the approach that labels RBCs, the fraction of labeled red blood cells and estimations of homogenous cell mixing must be known with great certainty to avoid errors with the calculation of RBC flux. It also does not account for non-linear flow estimations in capillaries such as the Fåhræus effect or plasma skimming in capillaries [59,60].

Fluorescently labelling blood cell plasma [57] has also shown promise, especially provided that both sodium fluorescein and indocyanine green have approval for use in the clinic. However, sufficient plasma space between the cells is required to provide contrast. As we show in Fig. 4, when blood cells are tightly packed, there is not enough plasma to provide optical contrast between two adjacent cells. Increasing the visible imaging power is not an option due to phototoxicity constraints. Therefore, plasma labeling approaches may

Biomedical Optics EXPRESS

undercount the true number of passing blood cells or limit/bias observations only to vessels with slower velocity or low capillary hematocrit.

The label free approach using split-detector not only leaves blood in its natural rheological state but also would benefit translational approaches that would ultimately seek to measure blood cell flux and image RBC morphology in the clinic.

4.2 Importance of objective measures of capillary RBC flux

At the tissue level, oxygen content and the number of passing blood cells are more important determinants of perfusion at the capillary level than blood velocity alone [61,62]. Other approaches have been successful at measuring capillary velocity in the living retina [22–24], but velocity by itself is not a direct estimator of RBC flux. As shown in Fig. 5, capillaries can have similar velocity but dramatically different RBC flux. This discrepancy is due to capillary specific changes in local hematocrit (volume ratio of RBCs: blood) [63,64]. This observation lends an important stride forward for the study of plasma skimming in capillaries of the normal and diseased retina. We also underscore the importance of directly measuring RBC flux. Capillaries have highly non-linear flow properties [59,60], and our measurements show that measures of diameter alone are weak predictors of RBC flux.

4.3 Comparison to other measurements of blood flow and velocity

Several approaches using adaptive optics have been able to extract blood velocities without contrast agents. In capillaries this has been possible using 2D scanning [19,22–24]. As shown by Zhong and colleagues [20], the measurement of velocities in arterioles and venules has been possible using 1D line scan imaging. Together, previous adaptive optics techniques have provided measures of blood velocity and calculations of large vessel flow. To the best of our knowledge, we present the first detailed images and counts of blood cell flux in retinal capillaries.

Similar strategies using Optical Coherence Tomography (OCT) combined with adaptive optics scanning ophthalmoscopy has also shown utility to visualize the retinal vasculature and obtain velocity measurements in arterioles and venules using 1D line scan [65,66]. OCT angiography has provided a transformative tool to map vascular perfusion at the structural and qualitative functional level [67]. OCT angiography generally relies on cell motion to generate vascular contrast, therefore vessel leakage or regions of non-perfusion are not visible. Using AOSLO, we are able to resolve microvascular structure regardless of functional perfusion (Fig. 3). This contrast will be important for studying vascular disease where collapsed or ghost capillaries may still show plasma patency, but not RBC movement [10].

Another technique that has been successful at measuring blood flow and velocity in the living retina is laser Doppler flowmetry and velocimetry, based on the measurement on the frequency shift induced by scattered light [68]. This has been demonstrated to be a powerful tool to image blood flow in the living retina, but due to signal strength and resolution limits, single capillaries have not been studied. Doppler OCT and laser speckle contrast approaches are being developed to report retinal blood flow. However, measurements to date are indirect and have not yet provided quantitative readout of absolute capillary flow or flux in the retina [69–74]. OCT scans in other tissues, such as the brain, have provided measures of RBC flux, yet are invasive in their approach [72]. Further studies may now compare and contrast these flux measurements in the cortex and retinal capillaries to provide insight on the flux and control of these CNS tissues.

4.4 Horizontal and vertical vessels in split-detector and motion contrast images

In our split-detector configuration, vertical vessels (those orthogonal to the knife edge orientation) have diminished contrast and some of them cannot be distinguished at all (Fig. 11, white arrow). This effect was also reported by Chui and colleagues [42]. In split-detector imaging, blood cell contrast is biased in the direction parallel to the knife edge. In vertical

Biomedical Optics EXPRESS

vessels, like the one in Fig. 3(A), the direction of motion is orthogonal to the knife edge orientation. In this condition, the bright and dark boundaries of moving blood cells will temporally average-out to a nearly equivalent background level, reducing the intensity-based contrast. Yet in motion contrast, these vessels show high contrast because bright to dark temporal transitions yield a high motion contrast signal at the center of the capillary.

Similar to what was reported by Sulai and colleagues [75], in motion contrast images, horizontal vessels have a profile of the two parallel lines (Fig. 11, red arrowhead, e.g. parallel to the knife edge orientation). Here at the level of individual RBCs we can see the source of this double peak. At the RBC cell wall interface, the boundary of the RBCs is dark, the adjacent capillary wall is bright. As RBCs move, pixels close to the capillary wall impart a large change in pixel value as they transition from imaging either an RBC or plasma (Fig. 12(B)). These temporal variations yield a high motion contrast signal that appears as two lines parallel to the capillary wall. It is possible that the polarity of the vessel wall and an RBC is different due to the sign of the change in the index of refraction at each interface. Consistent with this origin of RBC contrast, capillaries with zigzag flow showed a third motion contrast peak in the middle of the capillary (data not shown) indicating motion contrast arises from blood cell boundary and not the vessel wall.

4.5 Potential limitations and improvements of the technique

One limitation of the approach in its current state is that we can only image a single vessel at a time. This limits analysis to serial capillary study. Additionally, 1D scanning alone does not provide a registration signal in two dimensions and retinal stability is thus important.

While the data in this study have been measured manually to benchmark utility, this workflow opens the door for the development of new segmentation algorithms that will be able to automatically identify and count blood cells. This will facilitate study of larger numbers of capillaries by removing the manual grader bottleneck. Finally, we recognize that an immediate improvement can be realized by combining line scan data in both the forward and return direction of the resonance scanner cycle. This would double the collection rate to 30.9 kHz and permit temporal data averaging by a factor of 2, thereby increasing SNR or providing a two-fold increase in the maximum temporal velocity that can be measured.

4.6 Applications

Here, the mouse preparation provided a robust model to benchmark the performance *in vivo*. The mouse model of retinal blood flow analysis provides a stable platform where studies can be performed for several hours in a single imaging session. Future studies will examine the impact of retinal disease, such as in a mouse model of diabetic retinopathy. Unlike histological studies in the mouse, in-vivo imaging can track the progression of these vascular biomarkers in the same retina over time. This approach will provide new ways to quantify blood flux, velocity and flow in response to physiological challenge and disease.

While this study demonstrated feasibility in the mouse, the path toward clinical deployment is not far away. Adaptive optics instruments are already used in the clinic and in basic research settings using similar instrument design and imaging power [21,75–77]. Furthermore, these identified biomarkers of flux and flow provide large amounts of data in a fraction of a second. Even a single second of data capture between saccades can image hundreds of blood cells, and report their velocity and flux and measure capillary diameter. These label free markers provide a new wealth of information regarding retinal health, structure and function.

This study lays the foundation for a myriad of studies that may now quantify new metrics of capillary hemodynamics and vessel structure in the living retina. The label-free parameters of RBC flux, velocity, rheology, local hematocrit and capillary diameter are intimately associated, but one parameter is not necessarily predictive of the other. For example, flux and capillary diameter are only weakly correlated (Fig. 10). Using approaches described in this

Biomedical Optics EXPRESS

report, future studies will examine these metrics in the early and progressive stages of vascular disease in the retina. The study of these metrics may also provide critical information on the efficacy of new interventional treatments and pharmaceuticals that could fast-track the development of new corrective or prevention therapies for vascular disease of the eye; the leading causes of blindness in the developed world [4].

Funding

We appreciate the support from the following sources: NIH Grants EY001319 and F32EY023496, Research to Prevent Blindness Career Development Award (Schallek), Research to Prevent Blindness Stein Innovation Award, and an Unrestricted departmental grant from the Research to Prevent Blindness (New York, NY), the Schmitt Program on Integrative Brain Research, and Canon Inc.

Acknowledgments

We would like to thank David Williams, Vigneshwar Subramanian, Jay Helt, Jennifer Strazzeri, Keith Parkins, Jie Zhang, Ken Cheong and Robin Sharma, and for their assistance and feedback on this work.